On the fracture behavior of cortical bone microstructure

The effects of morphology and material characteristics of bone structural components

Allahyari, P.; Silani, M.; Yaghoubi, V.; Milovanovic, P.; Schmidt, F. N.; Busse, B.; Qwamizadeh, M.

DOI
10.1016/j.jmbbm.2022.105530

Publication date
2023

Document Version
Final published version

Published in
Journal of the mechanical behavior of biomedical materials

journal of the mechanical behavior of biomedical materials 137 (2023) 105530

Contents lists available at ScienceDirect

Journal of the Mechanical Behavior of Biomedical Materials

journal homepage: www.elsevier.com/locate/jmbbm

On the fracture behavior of cortical bone microstructure: The effects of morphology and material characteristics of bone structural components

P. Allahyari [a], M. Silani [a,*], V. Yaghoubi [b], P. Milovanovic [c], F.N. Schmidt [d,e], B. Busse [d,e], M. Qwamizadeh [d,e,**]

[a] Department of Mechanical Engineering, Isfahan University of Technology, Isfahan, 84156-83111, Iran
[b] Structural Integrity & Composites, Faculty of Aerospace Engineering, Delft University of Technology, 2629 HS, Delft, Netherlands
[c] Center of Bone Biology, Institute of Anatomy, Faculty of Medicine, University of Belgrade, 11000, Belgrade, Serbia
[d] Department of Osteology and Biomechanics, University Medical Center Hamburg-Eppendorf, 22529, Hamburg, Germany
[e] Interdisciplinary Competence Center for Interface Research (ICCIR), University Medical Center Hamburg-Eppendorf, 22529, Hamburg, Germany

ARTICLE INFO

Keywords:
Cortical bone
Extended finite element method (XFEM)
Bone microstructure
Fracture
Cement line
Sensitivity analysis

ABSTRACT

Bone encompasses a complex arrangement of materials at different length scales, which endows it with a range of mechanical, chemical, and biological capabilities. Changes in the microstructure and characteristics of the material, as well as the accumulation of microcracks, affect the bone fracture properties. In this study, two-dimensional finite element models of the microstructure of cortical bone were considered. The eXtended Finite Element Method (XFEM) developed by Abaqus software was used for the analysis of the microcrack propagation in the model as well as for local sensitivity analysis. The stress–strain behavior obtained for the different introduced models was substantially different, confirming the importance of bone tissue microstructure for its failure behavior. Considering the role of interfaces, the results highlighted the effect of cement lines on the crack deflection path and global fracture behavior of the bone microstructure. Furthermore, bone micromorphology and areal fraction of cortical bone tissue components such as osteons, cement lines, and pores affected the bone fracture behavior; specifically, pores altered the crack propagation path since increasing porosity reduced the maximum stress needed to start crack propagation. Therefore, cement line structure, mineralization, and areal fraction are important parameters in bone fracture.

The parameter-wise sensitivity analysis demonstrated that areal fraction and strain energy release rate had the greatest and the lowest effect on ultimate strength, respectively. Furthermore, the component-wise sensitivity analysis revealed that for the areal fraction parameter, pores had the greatest effect on ultimate strength, whereas for the other parameters such as elastic modulus and strain energy release rate, cement lines had the most important effect on the ultimate strength. In conclusion, the finding of the current study can help to predict the fracture mechanisms in bone by taking the morphological and material properties of its microstructure into account.

1. Introduction

Many individuals are at an increased risk of fractures, which have substantial social and economic consequences (Hernlund et al., 2013). Therefore, the study of bone materials is progressing quickly to better understand the skeletal system and facilitate new clinical approaches to predict fracture susceptibility of bones. Since the skeletal system is one of the primary structural components of the body, it is critical to establish new research models to further elucidate the mechanisms of bone fracture.

Bone is a heterogeneous, multiphase, and anisotropic material. A typical long bone consists of cortical and trabecular bone compartments (Fig. 1). Cortical bone with its dominant role in load bearing (Pistoia et al., 2003) is a highly complex composite that attains its unique combination of strength and toughness through deformation and toughening mechanisms at multiple length scales throughout its hierarchical framework (Zimmermann et al., 2014). Aging- and disease-related factors are known to alter the structure of bone at all

* Corresponding author.
** Corresponding author. Department of Osteology and Biomechanics, University Medical Center Hamburg-Eppendorf, 22529, Hamburg, Germany.
E-mail addresses: silani@iut.ac.ir (M. Silani), m.qwamizadeh@uke.de (M. Qwamizadeh).

https://doi.org/10.1016/j.jmbbm.2022.105530
Received 1 August 2022; Received in revised form 29 September 2022; Accepted 14 October 2022
Available online 22 October 2022

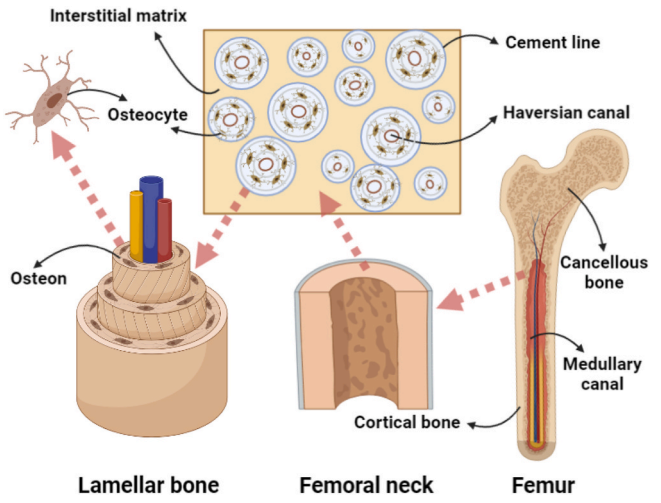

Fig. 1. Long bone anatomy of an exemplary, proximal, femoral bone at various length scales.

levels of its hierarchy, thereby raising the risk of fracture (Mulhern, 2000; Rho et al., 2002; Yoshino et al., 1994; Schmidt et al., 2019). One of the main aspects is the accumulation of microcracks. If not removed, microcracks accumulate over time and interconnect to form larger cracks, which may eventually lead to a bone fracture. Therefore, a key aspect of maintaining bone's mechanical properties is its ability to remodel and repair damaged tissue by replacing the damaged bone with cylindrical units of new bone. These newly formed cylindrical bone units (i.e., secondary osteons) are surrounded by cement lines, which apparently serve as a highly mineralized and stiff interface between the remaining bone material (interstitial bone) and the remodeled bone material (Fig. 1). This interface layer is typically 2–5 μm in thickness, is highly mineralized compared with interstitial bone (Milovanovic et al., 2018), and is called cement line or cement sheath (Cowin and Hegedus, 1976). Furthermore, inside the osteons, there are small holes called osteocyte lacunae containing the bone cells with the duty of mechanotransduction and mechanosensation of the loads imposed to the bone and sending the signals of bone formation or bone resorption to the bone surface but here in the current study, the main focus is on the cement lines and their properties on bone fracture behavior.

Cement lines are thought to play a crucial role in the micromechanical properties of bone (Schmidt et al., 2019; Zimmermann et al., 2009; Zimmermann and Ritchie, 2015), but their exact functions are complex and still insufficiently understood. Cement lines can serve as local stress concentrators to initiate cracks (Bonivtch et al., 2007; Nicolella et al., 2006); on the other hand, they can dissipate energy and act as barriers to slow down the propagation of microcracks by crack deflection (Zimmermann and Ritchie, 2015; O'Brien et al., 2003). Growing cracks have been observed to be deflected at cement lines, which increases bone toughness at the sub-macroscale (Zimmermann and Ritchie, 2015). Cement lines can also affect local bone mechanical properties (Kaya et al., 2017), which affect bone strength directly. The composition of cement lines has long been a subject of debate (Milovanovic et al., 2018; Bala and Seeman, 2015) as to whether they are mineral-rich (Boyde et al., 1990; Kingsmill and Boyde, 1998; Skedros et al., 2005) or mineral-deficient (Burr et al., 1988; Schaffler et al., 1987). The lack of agreement even on the basic composition of cement lines has likely hampered in-depth evaluation concentrating on their mineralization degree. However, from a microcompositional point of view, it has been shown that cement lines have a higher mineral content compared with osteon and interstitial bone, as shown by backscattered electron imaging and Raman spectroscopy (Milovanovic et al., 2018).

Over the recent few decades, research of biological materials, particularly bone tissue, has attracted much interest, and two/three-dimensional structural models of bone have been developed (Schmidt et al., 2017, 2019; Milovanovic et al., 2014, 2015; Li, 2013; Zimmermann et al., 2011, 2015, 2016). Studying the ultrastructural levels of bone, which have an enormous impact on its mechanical behavior, is limited to destructive methods, which do not allow to evaluate stress and strain distribution within the materials' volume, or temporal sequence of the underlying mechanisms. In contrast, finite element method (FEM) enables simulation studies to further understand and model processes of bone mechanics such as crack and fracture mechanisms, and clarify the impact of changes in composition and structure on the fracture behavior of bone. For simulation purposes using the extended FEM (XFEM), numerical models to investigate the deformation and failure of bone have been developed (Li et al., 2013, 2014; Gustafsson et al., 2019a, 2019b; Idkaidek and Jasiuk, 2017 ; Baptista et al., 2016). The biomimetic bone has also been computationally modeled using the FEM approach (Baptista et al., 2016) and it was found that small microcracks could be absorbed by osteons, but aspects such as the ratio between the size of an osteon and its distance from the crack, as well as crack angle and vertical distance of the crack in relation to the osteon, play a critical role (Gustafsson et al., 2019a, 2019b; Baptista et al., 2016). Interestingly, if an osteon is softer than the interstitial matrix, the cracks may be attracted by the osteon (Baptista et al., 2016).

The development of computational methods for fracture has been studied for decades. Numerous approaches have been introduced to model crack and damage in brittle and quasi-brittle materials. Element deletion techniques are one of the easiest but least accurate approaches to model discrete cracks (Pandolfi and Ortiz, 2012). In interelement-separation techniques, cracks are only allowed to develop along existing element edges. This limitation endows the method with comparative simplicity, but can result in an overestimation of the fracture energy when the actual crack paths are not coincident with element edges (Xu and Needleman, 1994). The results depend severely on the mesh size (and form of the chosen element) and the mesh bias that can be compensated only by computationally expensive remeshing. Embedded elements (EFEM) remove the need for remeshing (Jirásek, 2000). They are based on enrichment at the element-level that can be condensed out resulting in computationally efficient approaches. The extended finite element method (XFEM) is based on the partition of unity concept, uses nodal enrichment and is therefore more flexible than EFEM (Belytschko and Black, 1999; Moës et al., 1999). It was originally developed to model arbitrary crack growth without remeshing but was extended to numerous applications involving quantum mechanics, fluid-structure interaction, biofilm growths, two-phase flow, just to name a few. XFEM is commonly used together with the level set method (Osher and Sethian, 1988). Level sets are used to efficiently describe the crack surface. Phase field method developed by Miehe et al. (2010) shows promising feature of dealing with arbitrary crack evolution in 2D and 3D. However, phase field models are computationally more expensive as the crack is diffused over a certain width and modeled through phase field parameters that are added as additional degrees of freedom in the entire discretization. Besides that, there are also some meshfree-based methods, such as the Cracking Particle Method for modeling discrete cracks (Rabczuk and Belytschko, 2004; Rabczuk et al., 2010). This method represents crack growth discretely by activating crack surfaces at individual particles. Recently, another promising method for modeling pervasive material failure and fracture called Peridynamics was introduced, which is basically a nonlocal extension of continuum mechanics (Silling, 2000; Silling et al., 2007; Silling and Lehoucq, 2010). Like other meshfree and particle methods, Peridynamics utilize a point-based approximation and discretization constructed directly in the physical domain without fixed mesh connectivity. For a comparative review of Peridynamics and phase-field models for modeling fracture, please refer to (Diehl et al., 2022). In this paper, we used XFEM for modeling fracture in cortical bone for two main reasons: first, it is faster and more efficient than other methods, and second, it is already implemented in Abaqus.

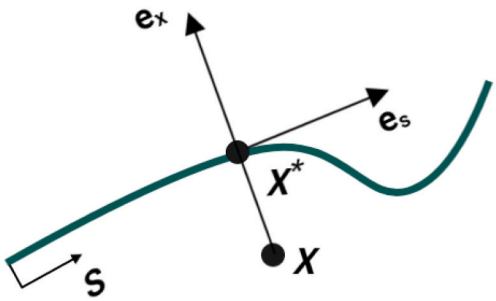

$$H(x) = \begin{cases} +1 & ;(x - x^*).e_n > 0 \\ -1 & ;(x - x^*).e_n < 0 \end{cases}$$

(a)

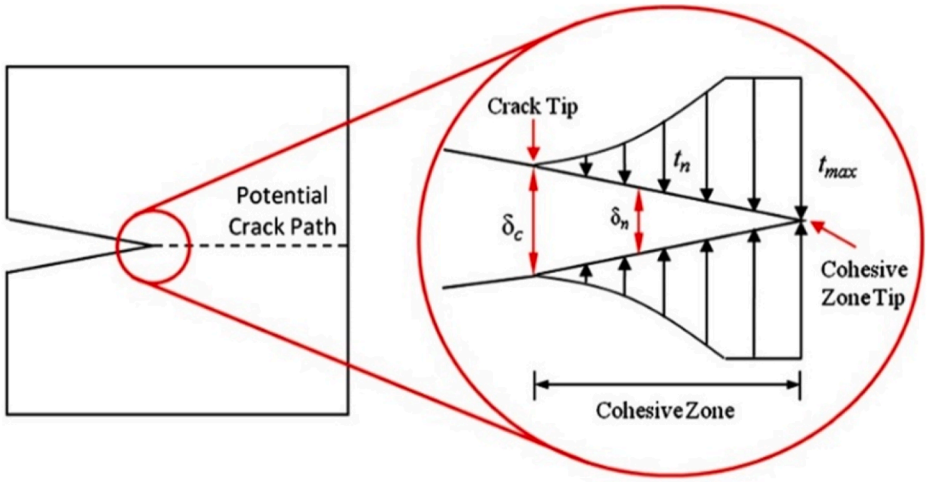

(b)

Fig. 2(a). The crack path tangential and vertical vectors; **(b)** a schematic model of the cohesive area and related failure.

Clearly, there are two dominant "philosophies" regarding the mechanical properties of cement lines. While Wang, Li (Wang et al., 2020) modeled cement lines as an elastic material with a lower modulus compared with the surrounding bone, multiple studies have shown higher values for the stiffness of cement lines (Milovanovic et al., 2018; Boyde et al., 1990; Kingsmill and Boyde, 1998). Additionally, cement lines become hypermineralized, and their degree of mineralization is not constant but varies with the tissue age of the osteon (Milovanovic et al., 2018). However, most of the computational studies so far have assumed a lower mineralization content of the cement lines, which has likely affected the observed crack propagation patterns (Li et al., 2013; Wang et al., 2020). Therefore, considering their drawbacks, those models cannot address the effects of cement lines as the stiff interface in the bone structure on the crack propagation path, which is important to understand the fracture mechanisms in the cortical bone.

The aim of this study was to use XFEM to improve our understanding of the fracture properties of cortical bone tissue. In the present study, the crack propagation behavior related to the contact surface between osteons, cement lines, and interstitial bone was simulated using the traction-separation law and mainly based on the bilinear cohesive zone model, addressing experimentally measured mineralization content of osteons and cement lines separately. Therefore, XFEM models were developed based on the experimental mineralization data. The effects of bone tissue microstructural parameters (such as areal fraction of osteon, cement line and pores, cement line mineralization, interstitial matrix, and osteon properties) on crack growth were additionally addressed to further adapt the model to the biological tissue. The innovation of our approach includes an examination of local sensitivity to the effect of input parameters on ultimate bone strength. The term "sensitivity analysis" refers to the calculation of the extent to which the predicted behavior for bone load-bearing capacity is affected by the values of independent input variables with uncertainty, such as the areal fraction or the mechanical properties of the material, which vary within a certain range for each component. Developing appropriate models allows for significant reductions in response time and, as a result, computational costs while guaranteeing the necessary accuracy in response.

2. Material and methods

Bone specimens were obtained from 10 female organ donors. The samples were taken from the subtrochanteric region. All samples were dehydrated and subsequently embedded in PMMA as described elsewhere (Milovanovic et al., 2015; Bernhard et al., 2013; Hahn et al., 1991). The samples were ground to coplanar specimen allowing for quantitative analysis after subsequent polishing of the bone surface. Prior to scanning electron microscopy (SEM), the samples were carbon-coated, and backscattered electron mode was used to obtain bone images.

To model the bone microstructure according to the obtained bone images of cortical samples for computational study, a best-fit function

was used to fit the distributions of the osteonal system's parameters, including osteon profiles (each specified as a circle), the surrounding thin layer of cement lines, and concentric Haversian canals (assumed to have a circular form). Finally, MATLAB software was used to produce models with randomly distributed cortical bone microconstituents depending on the data collected for each bone sample. The iterative process was repeated until the resulting microstructure models met all of the statistical distributions of the osteonal parameters as well as the areal fractions of the microconstituents of the respective backscattered electron images.

2.1. Quantitative backscattered electron imaging (qBEI)

As the mineral content is a crucial contributor to the tissue behavior (Currey, 1984, 2002), a quantitative analysis of the mineral content was performed. The degree of mineralization in osteonal bone and cement lines was measured with quantitative backscattered electron imaging (qBEI). For the quantitative analysis, data from 200 osteons was evaluated.

qBEI was carried out on an SEM device (LEO 435 VP, LEO Electron Microscopy Ltd., Cambridge, England) equipped with a backscattered electron detector (Type 202, K.E. Developments Ltd., Cambridge, England). The accelerating voltage was set to 20 keV, and a current of 680 pA and a fixed working distance of 20 mm were used (Milovanovic et al., 2014, 2015; Koehne et al., 2013). Image acquisition was carried out at 400 × magnification at a spectral range of 256Gy values and a spatial resolution of 0.3 μm per pixel.

Osteons were chosen within the cortex of the cross-section of the femoral bone. As a positive selection criterion, osteons had to exhibit a centrally located Haversian canal and a transverse section plane indicated by a circular shape. Gray values were calibrated to a calibration standard with carbon and aluminum (MAC Consultants Ltd., England) (Koehne et al., 2014), and a linear relationship between gray value and calcium content was assumed (Roschger et al., 1998). Hence, qBEI provides a measure of the calcium content reflected by gray values. For each osteon, cement line and osteonal bone tissue were separated manually and subsequently evaluated with respect to their mean gray values using a custom made MATLAB routine (Riedel et al., 2017) to calculate the mean calcium content (Ca_{mean}) in weight percent [wt%] of the respective structure and tissue. Differences in calcium content between cement lines and osteonal bone tissue were evaluated using paired Student's *t*-test in SPSS version 15, with p-values lower than 0.05 considered statistically significant. Additionally, a ratio of the calcium content of the osteon has been calculated to relate it to the cement line calcium content (OSTEON/CL).

2.2. FEM modeling

Following the acquisition of qBEI images, a two-dimensional model of bone microstructure was created. The aim was to investigate the interaction between cortical bone and microcracks, and the effect of the cement line interface on crack propagation and the resulting macroscale responses using the XFEM. One of the most common methods for simulating crack propagation is to employ formulations based on the XFEM. To introduce nongeometric cracks, the XFEM employs modified functions with additional degrees of freedom. These functions and additional degrees of freedom theoretically add discontinuities in the displacement field and infinite stress to the FEM, obviating the requirement to geometrically insert cracks into the model.

The proposed XFEM displacement field is divided into two sections: one is the development of the FEM without addressing discontinuities and cavities, and the other one is the enrichment of the finite element approximation. Their relationships are shown in equation (1).

$$u^h(x) = \sum_{\substack{I \\ n_I \in N}} \varphi_I(x) u_I + \sum_{\substack{J \\ n_J \in N^g}} b_J \varphi_J(x) H(x) + \sum_{k \in K^1} \varphi_k(x) \left(\sum_l c_k^{l1} F_l^1(x) \right) + \sum_{k \in K^2} \varphi_k(x) \left(\sum_l c_k^{l2} F_l^2(x) \right) \quad (1)$$

In equation (1), b_J and c_k^l are the extra nodes' degrees of freedom; $F(x)$ is a two-dimensional displacement function near the crack tip; and $H(x)$ is a generalized Heaviside function, which is positive if x is placed on top of the crack, and otherwise is negative, as shown in Fig. 2(a). The nodes were selected in such a way that those belonging to the elements that have a common boundary with the crack and the crack tip was not located in that element could be distinguished by the function $H(x)$, and the nodes belonging to the elements in which the crack tip was located could be expressed by the function $F(x)$.

$$\mathrm{H(x)} = \begin{cases} +1 & ;(\mathrm{x} - \mathrm{x}^*).\mathrm{e_n} > 0 \\ -1 & ;(\mathrm{x} - \mathrm{x}^*).\mathrm{e_n} < 0 \end{cases}$$

When a fractured piece or material is loaded, energy dissipation occurs. Microcracks and local deformation in the material cause this energy loss, which often occurs in small areas known as the fracture region. This generally results in a strain-softening zone with a negative slope in the stress–strain curve. Modeling of the cohesive region is one of the approaches that simplify the relationships required to assess the fracture process while focusing on the crack tip area to express the fracture properties in the form of stress–strain by considering the softening zone. The cohesive zone model was selected as a powerful tool for understanding the failure process in this study.

To formulate the cohesive region into an FEM, the cohesive elements were inserted into the contact surface area of the elements. Ordinary structural equations determine the behavior of the material outside the cohesive zone. On the other hand, the cohesive elements have a particular traction-separation law. Surface stresses are related to relative displacements or separations at the surface where cracks may exist, according to the rule of contact surface separation. These stresses usually comprise a vertical component and two tangential components related to the crack's opening mode and displacement. The occurrence of cracks or damage is proportional to the strength of the contact surface or the maximum stress in the stress-separation curve. When the area below this graph equals the amount of critical failure energy, the stress decreases to zero, and new surfaces of crack are formed.

Fig. 2(b) schematically shows the first mode of fracture of a material, which is expressed by the normal traction of the cohesive zone (T) as a function of the relative displacement (δ) between the two surfaces in equation (2), where f is a function used to express the stress distribution along the crack surfaces in the cohesive zone. In this model, it was assumed that all of the fracture mechanisms can be approximated by two parameters: a) maximum stress or strength of the cohesive zone (σ_{max}), and b) critical displacement (δ_{max}). For the displacements greater than critical displacement, the cohesive surface loses its stress-bearing capacity, and consequently, cracks grow.

$$T_n = f(\delta) \quad (2)$$

In addition, G_c, which is the critical energy release rate or area below the curve $f(\delta)$, is given in equation (3) and can also be used as one of the parameters of the cohesive region in the softening zone.

$$G_c = \int_0^{\delta_{max}} f(\delta) d\delta \quad (3)$$

In general, damage in the cohesive region is based on the following fracture modes: the first mode (opening), the second mode (shearing), the third mode (tearing), and the combined mode displacements.

Abaqus provides the linear elastic fracture mechanics (LEFM) approach and the traction-separation cohesive behavior approach for

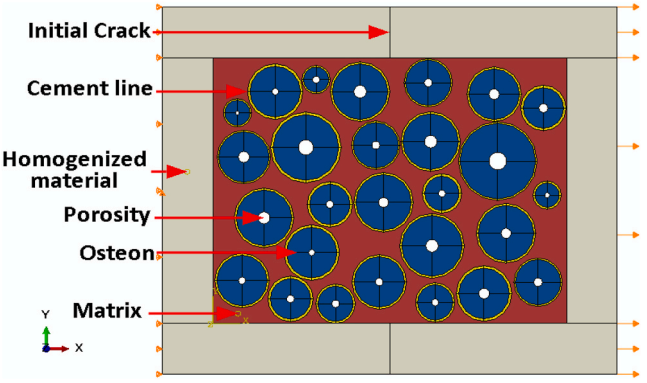

Fig. 3. Schematic model of the bone four-phase microstructure.

studying crack initiation and propagation using XFEM. The linear elastic fracture mechanics (LEFM) approach uses the modified Virtual Crack Closure Technique (VCCT) to calculate the strain energy release rate at the crack tip. The approach is more appropriate for brittle fracture problems. The traction-separation cohesive behavior is a general interaction modeling capability that can be used to model brittle or ductile fractures. The strain energy release rate at the crack tip is calculated based on the modified Virtual Crack Closure Technique (VCCT), which has been used to model delamination along a known and partially bonded surface.

In the XFEM-based cohesive segments method, cracks can initiate and propagate along an arbitrary, solution-dependent path in the bulk materials. It is in contrast with cohesive elements and surface-based cohesive behavior, which require that the cohesive surfaces align with element boundaries and the cracks propagate along a set of predefined paths. In the XFEM-based cohesive segments method, the near-tip asymptotic singularity is unnecessary, and only the displacement jump across a cracked element is considered. Therefore, the crack has to propagate across an entire element at a time to avoid the need to model the stress singularity.

Phantom nodes, superposed on the original real nodes, are introduced to represent the discontinuity of the cracked elements (Rabczuk et al., 2008). When the element is intact, each phantom node is completely constrained to its corresponding real node. When a crack cuts through the element, the cracked element splits into two parts. Considering the orientation of the crack, each part is formed by a combination of some real and phantom nodes. Each phantom node and its corresponding real node are no longer tied together and can move apart. The cohesive law governs the magnitude of the separation until the cohesive strength of the cracked element is zero, after which the phantom and the real nodes move independently.

When a crack cuts an element, the crack surfaces' compressive behavior must be considered. Abaqus's formulas for governing this behavior are similar to those used for surface-based small-sliding penalty contact. There are also some limitations in XFEM implementation in Abaqus. For example, the enriched element cannot have more than one crack, and the crack cannot turn more than 90 in one increment. The XFEM method is only available for first-order stress/displacement solid continuum elements and second-order stress/displacement tetrahedron elements but can handle both material and geometrical nonlinearity. All the mechanical constitutive models in Abaqus/Standard can be used in enriched elements.

Three different models were used to mimic the microstructure of bone tissue: homogeneous, three-phase, and four-phase composites. The interstitial bone as matrix, osteons as fibers, and Haversian canals as pores, which are described as empty cavities, make up the three-phase composite, while the four-phase composite contains the interstitial bone matrix, osteons, Haversian canals, and cement lines. Cement lines in the four-phase composite model surround the osteons and are located between the osteons and the interstitial matrix. Since the osteons in the studied models are long cylinders parallel to the longitudinal axis of the bone, two-dimensional plane strain assumptions can be considered (Abdel-Wahab et al., 2012).

According to Fig. 3, the model has dimensions of 0.9 mm × 0.725 mm × 0.3 mm (width × height × thickness). Of note, 0.1 mm on each side was considered a homogenous material in order to apply uniform deformation and reaction forces on both sides of the model. This value was chosen based on the size of the representative volume element. A tensile displacement of 0.009 mm in the horizontal direction was inserted to the right edge of the model. The left side was completely fixed in the horizontal direction, and only the midpoint was fixed in the vertical direction. An initial microcrack with a length of 0.1 mm was placed in the middle of the upper and lower borders in the direction perpendicular to the tensile displacement.

In the simulated model, linear quadrilateral plane strain elements were used. The mesh convergence study was performed using the size of different elements and the amount of ultimate strength as a convergence criterion. When the element size was greater than 0.004 mm, the ultimate strength value increased, and when the element size was in the range between 0.002 mm and 0.004 mm, the ultimate strength value converged. Therefore, for the current simulations, the element size of 0.003 mm was used for microstructural models.

2.3. Sensitivity analysis

The fundamental goal of sensitivity analysis is to determine how different components of a model affect the model's output. In fact, sensitivity analysis studies the "sensitivity" of the outputs of a system to changes in the parameters, inputs, or initial conditions, which are often poorly known. The outcomes can have an impact on model calibration, uncertainty assessment, and risk assessment. To analyze the model's structure, sensitivity analysis might be undertaken. When the parameters were defined in this study, sensitivity analysis was used to identify important and unimportant parameters for the simulations (De Pauw and Vanrolleghem, 2005). Sensitivity analysis can be divided into two large categories: local and global sensitivity analysis. Local methods perform sensitivity analysis at one specific point of the parameter space, whereas the global methods do the analysis in the whole parameter space (Vu-Bac et al., 2016; Hamdia et al., 2017). Since this work focus at developing a model with capability of prediction at one common operational point, the former was used in this study.

Given the general form of a system as equation (4):

$$\frac{dy}{dt} = f(y, \theta) \tag{4}$$

Where y is an n-dimensional vector of output variables, θ is the p-dimensional vector of input parameters (which can include the initial conditions y^0 and input variables), and t is the independent variable.

The sensitivity of an output parameter y to a parameter θ can be expressed as a sensitivity function (equation (5)). An output variable y is called sensitive to θ if small changes in θ produce significant changes in y. In contrast, a variable y is called insensitive to θ if changes in θ produce no changes in y.

$$S(t) = \frac{\partial y(t)}{\partial \theta} \tag{5}$$

Here, the finite difference approximation was employed to compute local sensitivities as follows (Bosnić and Kononenko, 2008):

$$\frac{\partial y_i}{\partial \theta_j} = \lim_{\Delta\theta_j \to 0} \frac{y_i(t, \theta_j + \Delta\theta_j) - y_i(t, \theta_j)}{\Delta\theta_j} \tag{6}$$

This equation is only valid if we consider an infinitesimal variation (perturbation) of the parameters, inputs, or initial conditions θ ($\Delta\theta_j \to 0$). Equation (6) shows that the application of the finite difference

Table 1
Mechanical properties of microstructural components and homogeneous material of bovine bone (Abdel-Wahab et al., 2012).

Model	Elastic modulus (GPa)	Poisson's ratio	Strain energy release rate (N/mm)
Homogenized material	10.46	0.167	0.422
Osteon	9.13	0.17	0.86
Interstitial matrix	14.122	0.153	0.238
Cement lines	6.85	0.49	0.146

Table 2
Mechanical properties of microstructural components and homogeneous material of human bone (Gustafsson et al., 2019b).

Model	Elastic modulus (GPa)	Poisson's ratio	Strain energy release rate (N/mm)
Homogenized material	10.46	0.167	0.422
Osteon	19.29	0.33	0.2
Interstitial matrix	22.183	0.29	0.2
Cement lines	33	0.27	0.2

method requires the solution of the model (equation (4)) using the nominal value of the parameters y_i (t, θ_j) and p solutions of the equations using perturbed parameters y_i $(t, \theta_j + \Delta\ \theta_j)$. It should be noted that only one parameter was perturbed at a time while all others were kept at their nominal value.

Practically, $\Delta\theta_j$ is defined as the value of the nominal parameter θ_j multiplied by a perturbation factor ξ chosen by the user, and y_i is the response function. The choice of this perturbation factor determines the efficiency of the sensitivity analysis. The partial derivative finite difference approximation is valid only if the perturbation factor is close to zero. This is true in theory, but never numerically due to the limited accuracy of the calculations. If the perturbation factor becomes too small, it will lead to numerical inaccuracy. On the other hand, $\xi\theta j$ should not be too large as the nonlinearity of the model plays an important role in the sensitivity calculation. In this study, the amount of perturbation factor ξ according to (Idkaidek and Jasiuk, 2017; Bosnić and Kononenko, 2008; De Pauw and Vanrolleghem, 2003) was taken as 0.0001.

3. Mechanical properties of bone constituents

In the current study, crack propagation in the bone microstructure was studied for two different tissues. In the first model, the parameters of microstructural constituents and homogenous properties of bovine bone were retrieved from the previously published experimental results (Abdel-Wahab, 2011). Furthermore, in the first model, Poisson's ratio of the cement line was chosen from a previous study (Abdel-Wahab et al., 2011). However, in the second model, the experimentally obtained properties of the human bone samples were used for the parameters of the microstructural constituents in the simulated representative volume elements (RVEs). Lakes and Saha (1979) demonstrated that cement lines exhibit isotropic viscoelastic behavior due to their particular chemical composition, and their elastic characteristics differ from those of osteons.

According to Budyn and Hoc (2006), the elastic properties of cement lines in the bovine bone model were regarded as 25% weaker than the elastic properties of osteons derived from nanoindentation tests (Budyn and Hoc, 2006). On the other hand, it has been reported that the elastic modulus of the cement lines is greater than that of osteons or interstitial bone (Milovanovic et al., 2018; Boyde et al., 1990; Kingsmill and Boyde, 1998; Skedros et al., 2005). Therefore, to investigate the effect of cement line on the crack path, the second model with the stiff properties of the cement line was simulated. Table 1 shows the elasto-damage properties of a bovine bone model (Abdel-Wahab et al., 2012; Abdel-Wahab, 2011), while Table 2 shows the elasto-damage properties of the human bone model (Idkaidek and Jasiuk, 2017; Nalla et al., 2006; Koester et al., 2011; Mischinski and Ural, 2011; Wang et al., 2017; Demirtas et al., 2016; Giner et al., 2017). It is worth noting that all microstructural elements were assumed to be isotropic. In the present study, FEM models based on representative volume elements (RVEs) of bone tissue on microscale were developed using the extracted input parameters.

Linear elastic behavior was determined for homogenous material and constituents of cortical bone microstructure. The elasto-damage criterion (Nalla et al., 2005) has been used to define failure in various biological materials, and the principal strain criterion (Bayraktar et al., 2004) has been used to study failure in human bone tissue. The highest principal strain could be used to predict the onset of fracture in these models. Equation (7) defines the fracture criteria f:

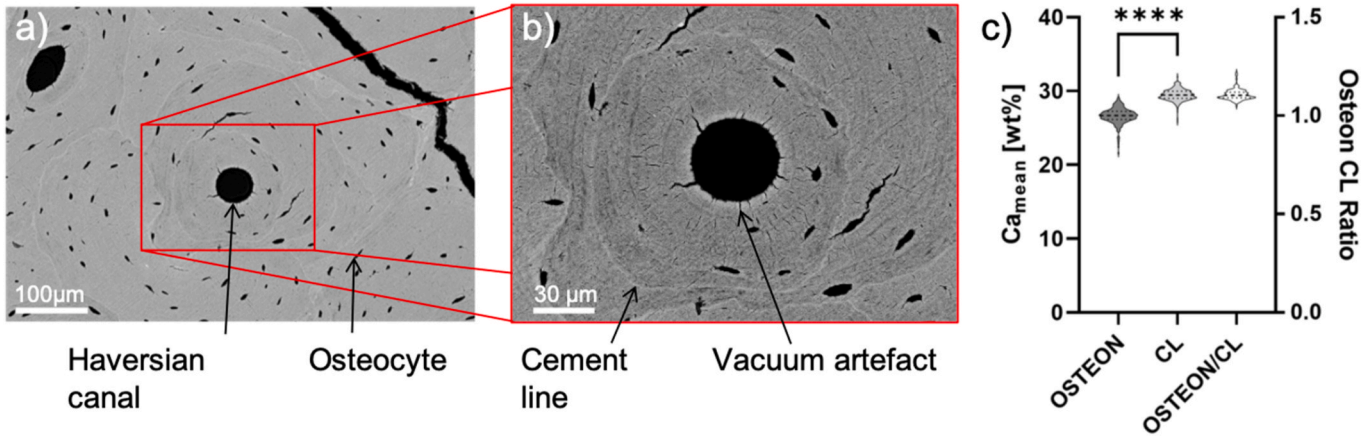

Fig. 4. (a) Results of the quantitative backscattered electron imaging: In the center of the image (red frame) an osteon with the surrounding cement line with lighter grey values and a central Haversian canal is depicted. Osteocyte lacunae are visible throughout the image. In the upper right corner, a clear crack, which was caused by the imaging modality in the vacuum chamber of the electron microscope is visible. **(b)** The middle image shows a highly contrasted section of the left image with clearly visible cement lines. Small cracks, e.g. radial at the Haversian canal, are found in the entire measurement area and are caused by the vacuum environment. **(c)** In the right graph, the violin plots show the calcium concentrations in the osteonal bone material and in the cement line, calculated from the gray value images. There is a clear, significant difference (**** Student's t-test: $p < 0.0001$). The mean calcium content in the cement lines is 10.66% higher than in the osteonal bone tissue. The right violin plot shows the relationship between the osteonal mineral content (OSTEON) and the mineral content of the cement line (CL) (right ordinate). 10% higher calcium content of the cement lines can be clearly seen from the mean of approx. 1.10.

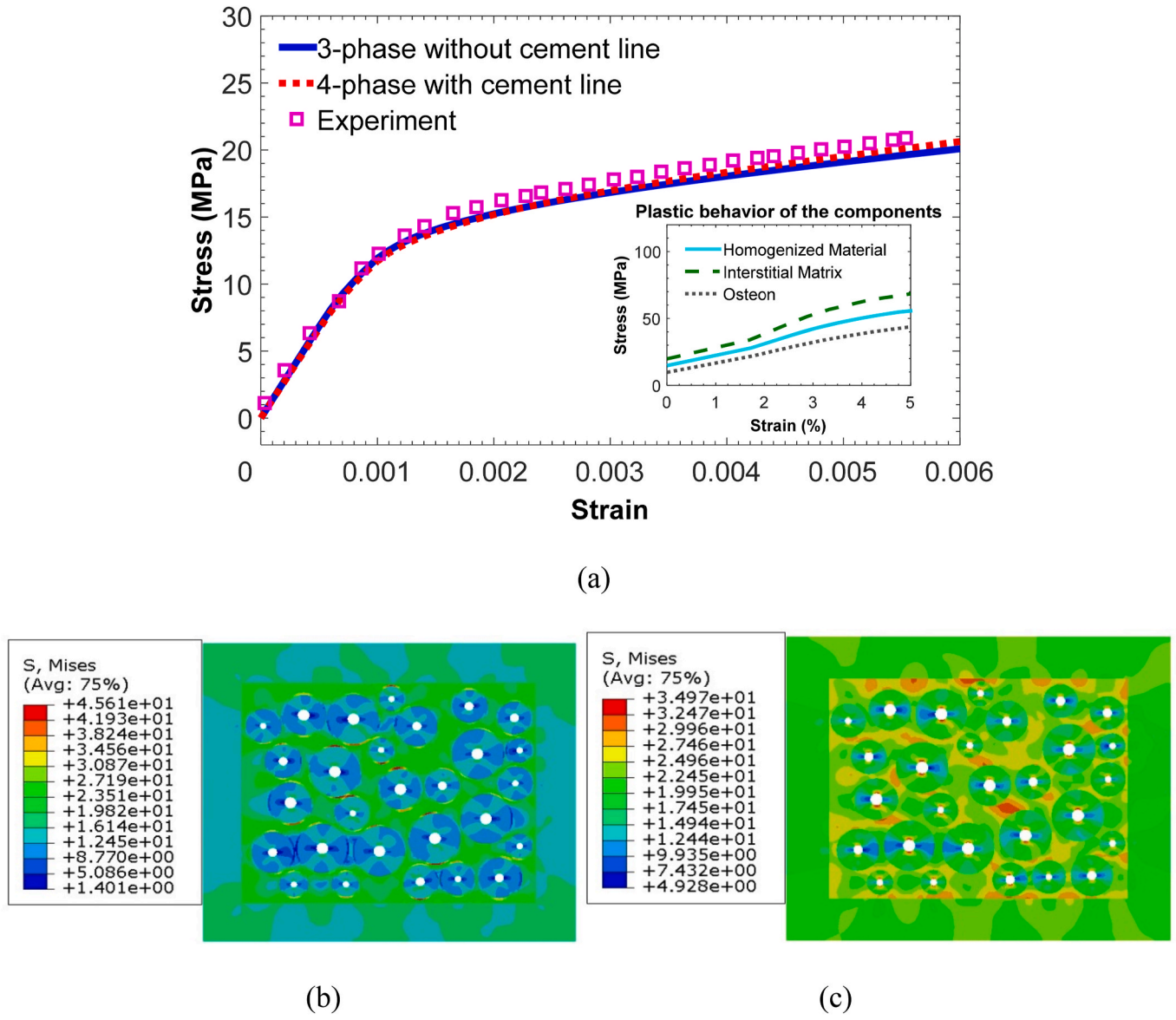

Fig. 5. (a) Comparison of the stress–strain behavior of two simulated models (three-phase and four-phase structures) with experimental results for the un-cracked medium, the von Mises stress distribution for the strain of 0.0056 in models **(b)** without cement lines, and **(c)** with cement lines (Abdel-Wahab, 2011; Abdel-Wahab et al., 2011).

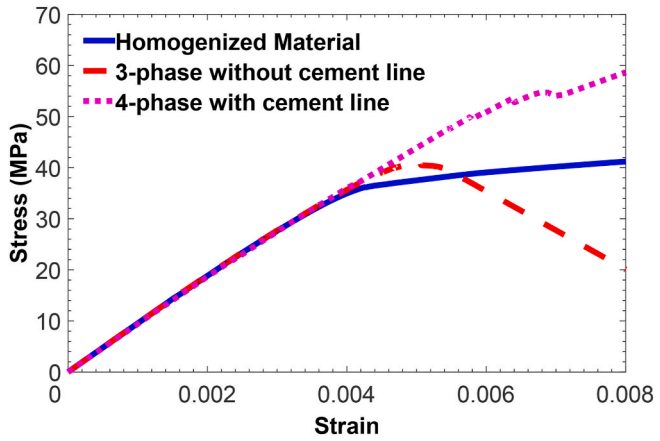

Fig. 6. Stress–strain diagram of homogeneous, three-phase, and four-phase composite microstructure models under tension for a cracked medium.

Table 3
Crack initiation conditions of the three-phase, four-phase, and homogeneous models.

Model	Stress (MPa)	Strain
Three-phase model	8.66	0.0009
Four-phase model	11.5	0.00122
Homogeneous model	8.21	0.00084
Simulation results of previous studies for a four-phase model (Abdel-Wahab et al., 2012)	12.85	0.00136

$$f_{MAXPE} = \left\{ \frac{\varepsilon_{max}}{\varepsilon^0_{max}} \right\} \tag{7}$$

Where ε_{max} is the maximum principal strain and ε^0_{max} is the critical strain of the onset of damage. It should be noted that damage begins when $f_{MAXPE} > 1$. The traction-separation law was utilized as a criterion for the beginning and development of damage in this study. In these models,

Table 4
The amount of stress and strain in the final state of crack for the three-phase, four-phase, and homogeneous models.

Model	Stress (MPa)	Strain
Three-phase model	41.37	0.005
Four-phase model	38.6	0.0041
Homogeneous model	31.62	0.0039
Simulation results of previous studies for a four-phase model (Abdel-Wahab et al., 2012)	39.44	0.0045

the onset of damage was determined by the maximum critical principal strain, which was set at 0.004 for microstructural components and homogeneous material, and the criterion for damage evolution was specified by the energy release rate (Rakovec et al., 2014).

4. Results and discussion

Ground sections of cortical femoral bone were imaged using qBEI (Fig. 4(a, b)). There was a significantly higher mean calcium content (Fig. 4(c)) in cement lines compared with osteonal tissue (cement lines: 29.45 ± 0.81 $wt\%_{Ca}$ vs. osteons: 26.62 ± 1.11 $wt\%_{Ca}$, $p < 0.0001$). The ratio of calcium content of the two tissues (cement line and osteonal bone tissue) showed 10.67% higher calcium content in cement lines (Fig. 4(c)), as reflected in their higher gray values in qBEI images (Fig. 4 (a, b)).

Calcium content determination using qBEI was validated (Roschger et al., 1998) more than 20 years ago and has since been applied and confirmed many times (Milovanovic et al., 2015, 2018; Busse et al., 2009, 2010). Therefore, based on gray values, we confirmed that cement lines have a higher mineral content than osteonal bone, as shown previously (Milovanovic et al., 2018). Furthermore, it has been shown that bone tissues hardness and modulus primarily depend on the mineral content of the tissue (Currey, 1988; Stockhausen et al., 2021; Schmidt et al., 2018). Therefore, the increased gray value (representing higher calcium content) and the known effect of mineralization on increasing elastic modulus and hardness (Schmidt et al., 2018) indicate a higher modulus and hardness of cement lines in human bone.

Elastic and plastic properties were determined for the microstructural components and the homogeneous material to validate the simulated microstructural models compared to the results obtained in (Abdel-Wahab et al., 2012). According to Fig. 5, no initial cracks were taken into account for validation of the results for three-phase and four-phase structures. Based on Fig. 5(a), which depicts the stress–strain behavior of the simulated models and the experimental data (Abdel-Wahab, 2011; Abdel-Wahab et al., 2011), the simulation results were consistent with the experimental results for cortical bone tissue in transverse directions. Hence, the numerical simulations were consistent and guaranteed that the simulated models were valid enough for further examinations. Both models based on elasto-plastic data showed similar behavior to the experimental results up to an approximate strain of 0.006 where the simulation was stopped. The model with cement lines (four-phase model) exhibited better agreement with the experimental findings than the three-phase model without cement lines. The plastic behavior of the materials (Abdel-Wahab et al., 2011) employed in the simulation is shown in a small plot in Fig. 5(a).

Fig. 5(b) and (c) demonstrate the von Mises stress distribution for tensile loading without cement lines and with cement lines, respectively.

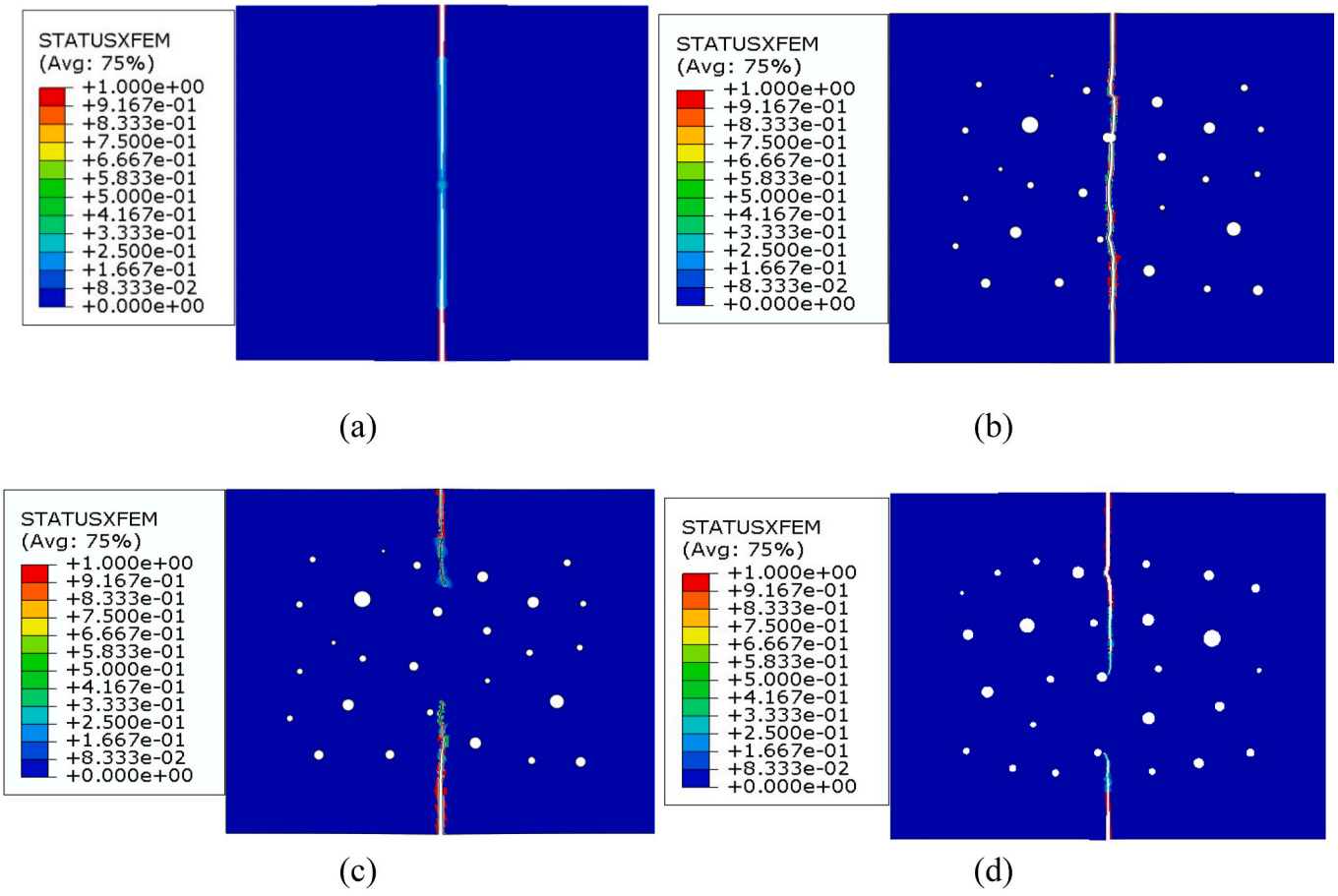

Fig. 7. Crack propagation paths in bovine bone for **(a)** the homogeneous model, **(b)** the model without the cement line, **(c)** the model with the thick cement lines, and **(d)** the model with the thin cement lines.

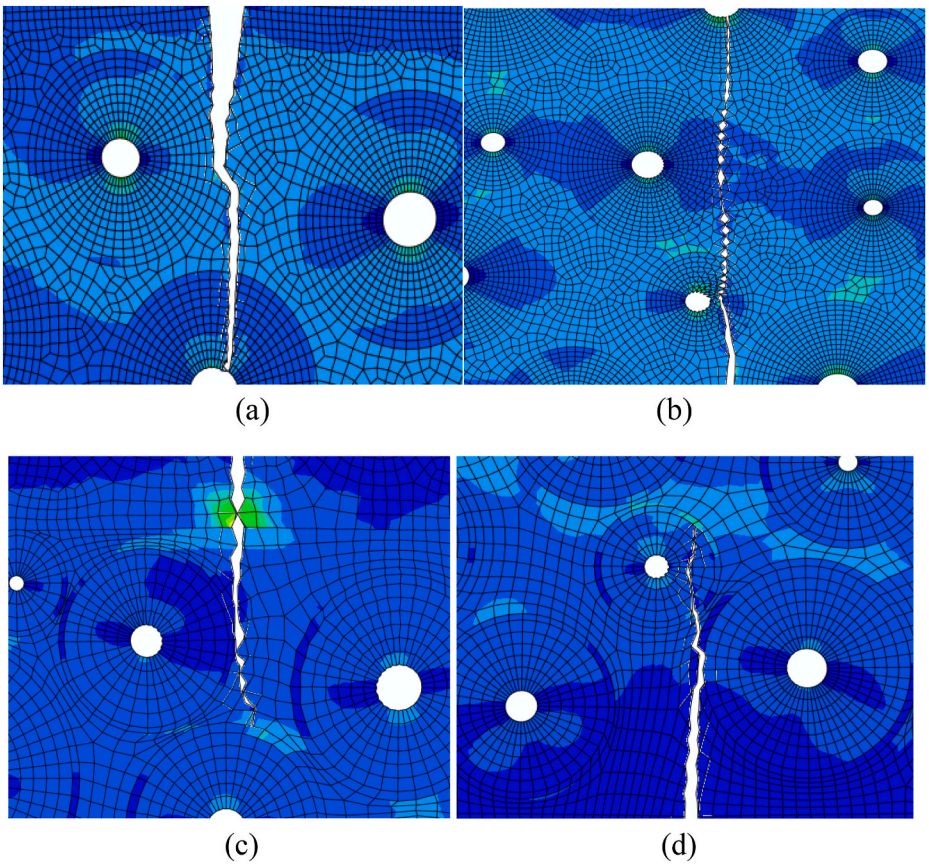

Fig. 8. (a) Upper microcrack propagation path, and **(b)** lower microcrack propagation path in the three-phase model; **(c)** upper microcrack propagation path, and **(d)** lower microcrack propagation path in the four-phase model.

These distributions are related to strain of 0.0056. Finite element simulations revealed that large local plastic zones formed at the interface between the osteon and the interstitial matrix in both the model with and that without cement lines. The interstitial matrix regions showed higher stress than the osteonal regions and the homogenous region in both the model with and the model without cement lines. Von Mises stress was larger if two osteons were located near to each other. The maximum stress values were recorded to the cement line area in the four-phase model with cement line. This suggests that cement lines are crucial in separating the osteon from the interstitial matrix, and they appear to be key bone components in protecting against fractures. According to our simulated models, cement lines play an essential role in the fracture process of bone microstructure, and the simulation results are in agreement with the experimental observations in terms of the effect of cement lines as osteon barriers (Mohsin et al., 2006).

Validated models with elasto-damage properties of bovine cortical bone were utilized to explore the fracture behavior of bone microstructure using XFEM. To examine the effect of microstructural features of bone tissue, particularly that of cement lines, three different models were developed: homogeneous, three-phase, and four-phase composite. Fig. 6 depicts the stress–strain behavior of the homogeneous, three-phase, and four-phase models investigated in this study. The three models' quasi-static analyses revealed significant differences in the overall behavior and fracture propagation paths. Before the crack initiated and propagated, the three obtained stress–strain curves behaved almost identically.

The homogenous model softened due to damage, and crack initiation occurred at low stress and strain values. In contrast, the four-phase model requires higher stress and strain to initiate a crack, whereas the three-phase model lies in between these two. The crack initiation status and final status of the crack (the final status for homogenous and three-phase models is the complete fracture, and for the four-phase model is when the crack stopped and does not propagate anymore) is presented in Tables 3 and 4. When the size of microcracks was examined as deformation increased, we found that cracks in the homogeneous model grew faster than cracks in both microstructural models. Although the criterion for initiating microcracks was the same for all three models, the heterogeneity of different microstructures caused different stress distributions, resulting in different stresses required to propagate the microcracks.

In the model without a cement line, osteons tended to have larger deformation with regard to the interstitial matrix than in the model with a cement line. This result may explain the further hardening process reported in other simulations (Budyn and Hoc, 2006). The homogeneous model showed the lowest fracture stress and strain values; the three-phase model had the highest values; and the four-phase model's behavior was between these two models, as shown in Table 4. The stress and strain derived from the analyzed models are compatible with the simulation results of prior investigations, as shown in Tables 3 and 4 (Abdel-Wahab et al., 2012).

The homogeneous model failed completely in the direction of microcrack growth because there were no obstacles to prevent the cracks from propagating under the applied load, as shown in Fig. 7(a). Due to Abaqus software's restriction in modeling multiple cracks in a single element, two cracks did not meet in two different directions in the last element. As shown in Fig. 7(b), the three-phase model entirely failed and showed the complete failure behavior, after which the stress–strain curve decreased and softening behavior was demonstrated.

However, the crack behaved differently in various simulations in the four-phase model. In several models, such as the one illustrated in Fig. 7 (c), the crack stopped as soon as it hit the cement line. The cement line also worked as a barrier against crack propagation, so the model was not

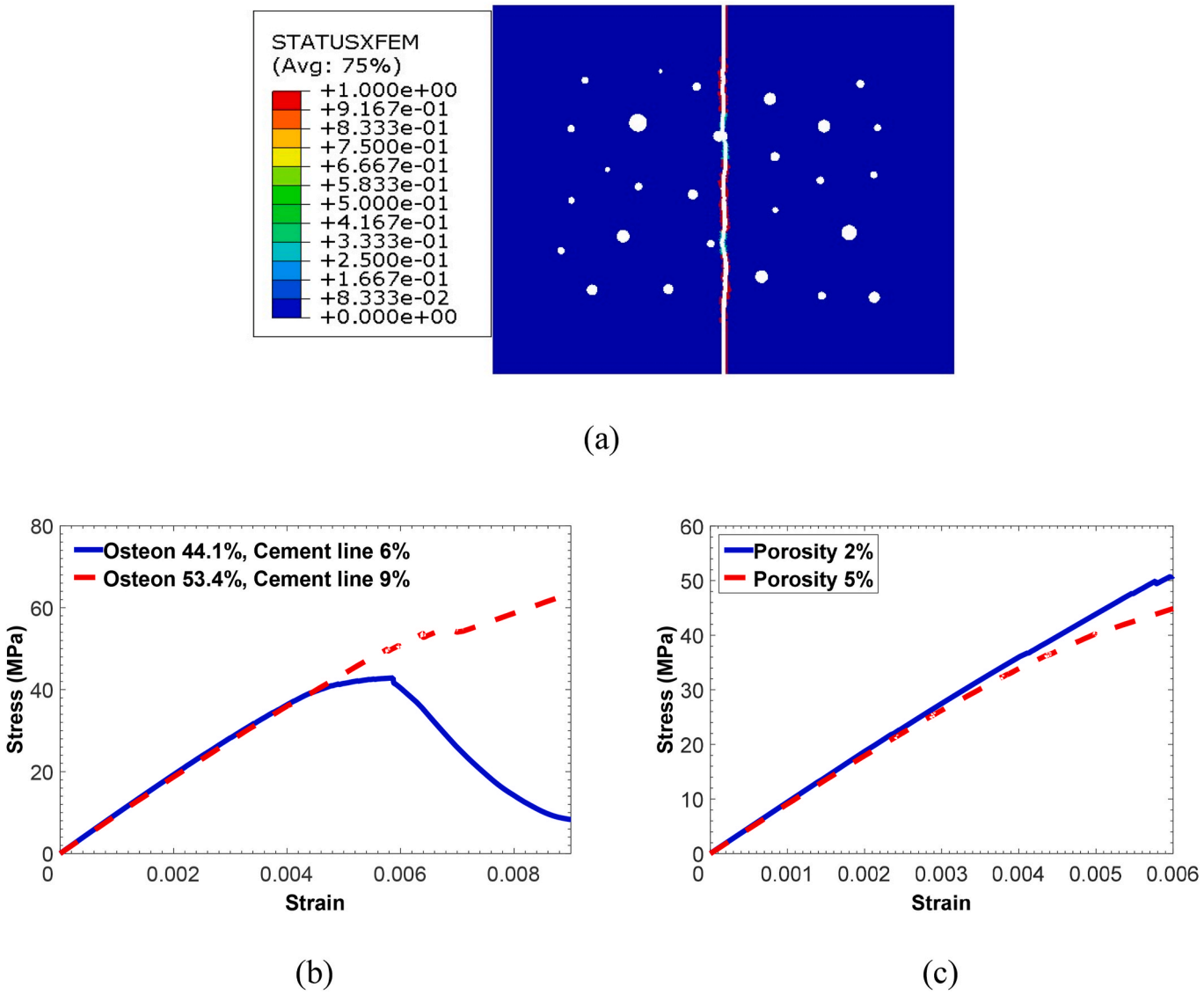

Fig. 9. (a) Crack propagation path in the four-phase model with a decrease in the percentage of osteon to the value of 44.1%; **(b)** the comparison of stress–strain diagrams of four-phase composite microstructure with different osteon percentage and cement line under tension; and **(c)** the effect of porosity (areal fraction of pores) on the stress–strain behavior of the bone microstructure.

completely damaged. In certain models with the same input parameters as the previous models but a different random distribution, the cracks penetrated the cement line and were deflected into the cavities by the osteons. These findings demonstrate that the mechanical properties of each component, as well as the microstructural distribution, are crucial in predicting the crack path. Almost all prior studies have considered that the stiffness of the cement line is lower than that of the osteon. However, according to our experiments on the human bone samples, the cement line has greater stiffness than the osteon and the interstitial matrix. Given that the thickness of the cement line in this study was 3–5 μm, we demonstrated that if the cement line in the crack path was thick enough, it could stop the crack growth. Fig. 7(d) shows how the crack can penetrate the cement line with a small thickness in the four-phase model. It was found that the stress–strain curve depicted the hardening behavior after the microcracks had been stopped, and the material that remained undamaged after this point exhibited an elastic response. These results confirm the importance of microstructure heterogeneity in the overall behavior of bone tissue. Hence, the crack can be stopped by cavities and cement lines, and the crack propagation path is perpendicular to the imposed displacement direction.

Fig. 8(a) and Fig. 8(b), which exhibit the crack growth path in the three-phase model of bovine bone tissue, revealed that the osteon phase affected the upper crack path. The upper crack stopped when it reached the cavity. The position and size of the internal cavities influenced the crack path, which is consistent with the numerical findings of previous studies (Najafi et al., 2007, 2009). The lower crack grew directly and resulted in full failure. The principal stress distribution was also affected by the presence or absence of a cement line. The microstructure of bone tissue was found to have a significant effect on crack propagation, which is consistent with the previous experimental results (Nalla et al., 2005). According to their findings, the microstructure has a considerably stronger impact on crack growth when the crack plane is perpendicular to the osteon axis. The features and characteristics of the cement line, on the other hand, have not been fully investigated experimentally and should be further determined.

According to Fig. 8(c), the upper crack was stopped by the cement lines in the four-phase model, and the lower crack was deflected towards one osteon before being stopped by its cement line (as shown in Fig. 8 (d)). These findings support the importance of the intermediate phase (cement line) in bone fracture and are consistent with previous

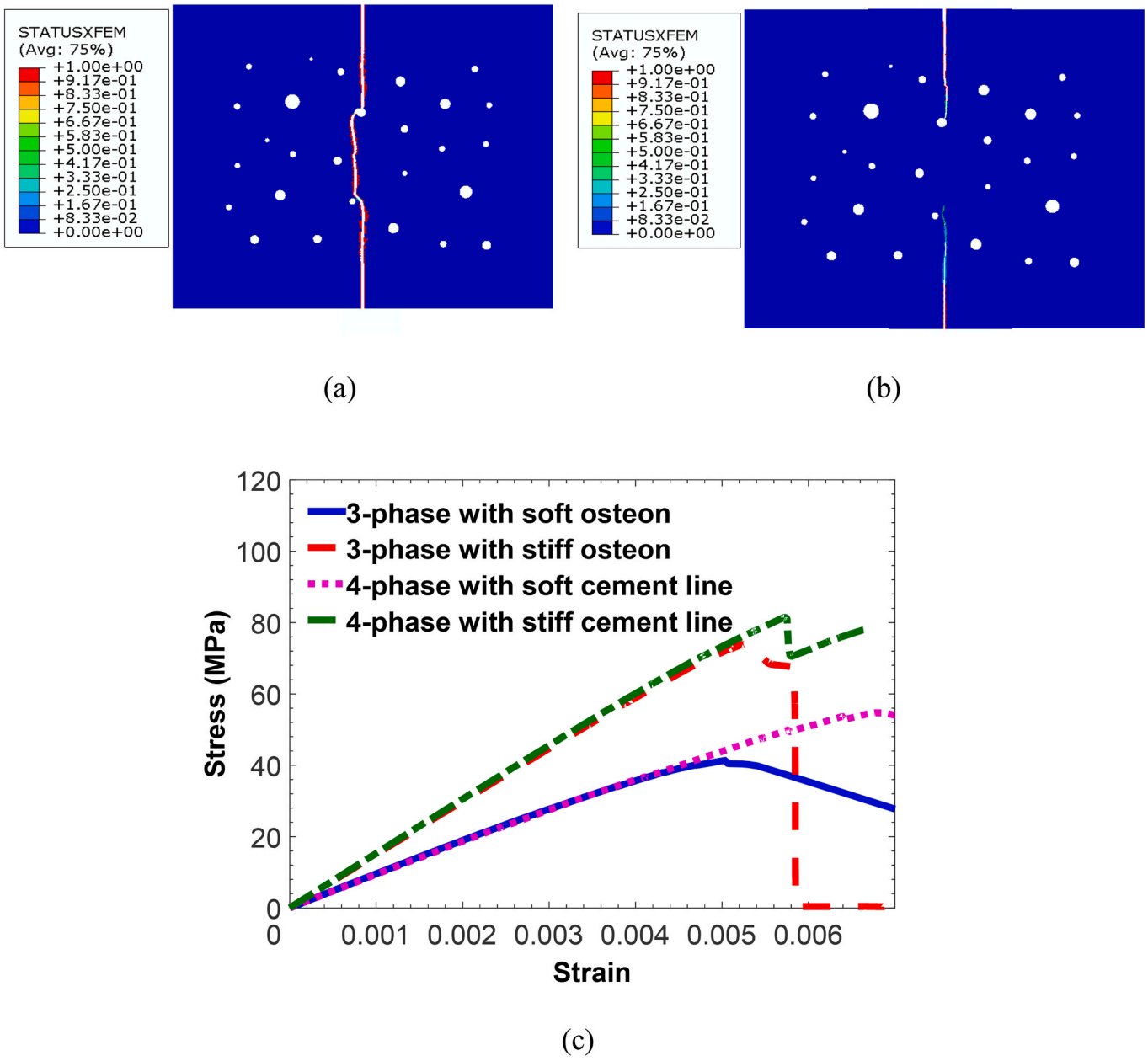

Fig. 10. Crack propagation path in **(a)** the three-phase model without cement lines and **(b)** the four-phase model with cement lines for mechanical properties of human bone; **(c)** stress–strain curve comparison of the three-phase model and the four-phase model with mechanical properties related to bovine and human bone according to Tables 1 and 2, respectively.

experimental findings (Mohsin et al., 2006). They examined short cracks and showed that cracks as small as 100–300 μm could be stopped by reaching the cement line. Also, in a recent study (Gustafsson et al., 2019b), a model with a single osteon was developed and it was shown that the strength of the cement line had a significant effect on the microcrack to assess the risk of fracture. They found that weak cement lines have the ability to deflect microcracks, while microcracks existing in models with stiff cement lines can penetrate the osteon by passing through the cement line.

Based on the reported areal fraction values of the osteon in a recent study (Wang et al., 2020), the areal fraction of an osteon was reduced to 44.1% in the other four-phase model shown in Fig. 9(a); it was observed that unlike in the four-phase model with a areal fraction of 53.4%, where the crack was stopped or deflected by the cement line, the crack in this case penetrated the cement line, and the model was completely broken. These findings highlight the importance of bone mineral density and osteon areal fraction in different groups of bone, including aged, healthy, and diseased bone. The fracture toughness likewise decreases in the model with increasing osteon fraction, according to the stress–strain curve illustrated in Fig. 9(b). Increased tissue porosity is one of the indicators of osteoporosis (Agnew and Stout, 2012). As shown in Fig. 9(c), when the Haversian canal derived pores' percentage increases, the principal stress is required to start the fracture, and also the fracture toughness decreases due to the fact that the pores impact the distribution of the principal stress. Crack growth curves revealed that microscale crack propagation typically occurs in locations with larger edge cavities and higher stress concentrations.

By varying the mechanical characteristics and applying the parameters of human bone tissue, two simulated microstructure models were examined. It should be observed that the elastic modulus for all components increased as the energy release rate decreased. The fracture process was the same in the three-phase and four-phase models as it was

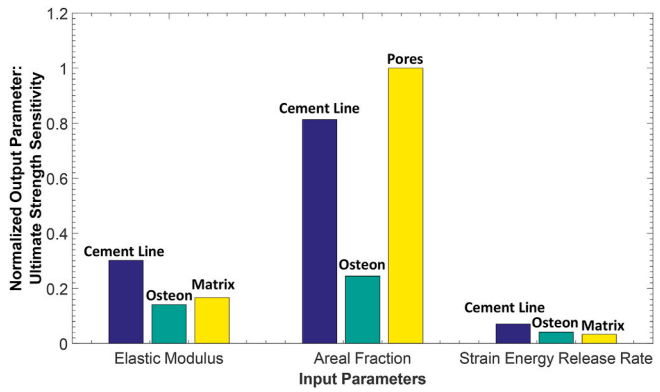

Fig. 11. Sensitivity analysis of bovine bone components with input parameters of elastic modulus, areal fraction, and strain energy release rate of the components, and the normalized output parameter of ultimate strength sensitivity.

in simulated models with mechanical properties related to bovine bone, so the model without cement lines was completely broken. However, in the model with cement lines, the lower crack was stopped by the cement line, while the upper crack was stopped by the cavity and did not fail completely. Fig. 10(a) and Fig. 10(b) depict damage in the three-phase and four-phase models with mechanical properties of human bone, respectively.

The stress–strain curves of the three-phase and four-phase models are shown in Fig. 10(c) by defining two types of mechanical properties of bovine and human bone according to Tables 1 and 2, respectively. In the three-phase model, the structure was completely fractured, and it is obvious that the fracture toughness was higher for human bone with mineralized osteon (stiff osteon). After the fracture point, very short softening behavior was observed for the human samples with stiff cement lines. Similarly, the fracture toughness was higher in the four-phase models of human samples with mineralized osteon and stiff cement lines. As shown in Fig. 10(c), the cement line significantly affected fracture properties of the bone microstructure. The stiffer and thicker the cement lines are in the bone microstructure, the more they could arrest crack growth at microstructural levels.

In this study, the effects of the elastic modulus and energy release rate of the cement line, osteon, and interstitial matrix, and areal fraction of the cement line, osteon, and pores as input parameters on ultimate strength as an output parameter were investigated using the local sensitivity method with finite difference approximation. This model can be used to assess how material stiffness and strength affect the toughness of cortical bone tissue on a small-length scale. The results demonstrated that the areal fraction of the components had the largest effect on the ultimate strength, while the strain energy release rate of the components had the smallest effect.

For further analysis, the effect of the parameters was investigated component-wise. As shown in Fig. 11, by comparing the areal fraction of the components, pores had the greatest impact on ultimate strength. Besides, among different components, the elastic modulus and energy release rate of the cement line showed the largest impact on ultimate strength, suggesting that cement lines are a very important component in bone morphology (Fig. 11). The suggested model is a useful tool for analyzing how local changes in input parameters related to aging and the effects of bone health can influence cortical bone fracture resistance.

5. Conclusion

Cement lines with their controversial organic and inorganic composition are thin boundaries surrounding the osteons. It is expected that the cement line become hypermineralized with the increase in the tissue age of the osteon. Therefore, calcium content of osteons and their corresponding cement lines was measured in human cortical bone from subtrochanteric femoral samples. The qBEI analysis revealed that the cement line had a higher calcium content than the corresponding osteonal area, highlighting the necessity of studying the effect of cement line material characteristics and areal fraction on the fracture behavior of bone microstructure. Using the XFEM, a variety of finite element models were developed based on the results of previous experiments to assess the deformation and fracture of cortical bone tissue. We determined that the developed models produced high-quality results while also adequately reflecting the experimental data.

Based on the results of numerical simulations, the stress–strain behavior differed between the homogenous, three-phase, and four-phase models. Despite the cement line as an intermediate phase, the propagation of microcracks requires additional stress and strain. The homogeneous model showed the lowest strength, whereas the three-phase model had the highest. When the three-phase and four-phase models were compared, it was discovered that in the four-phase model, the cement lines in the path of crack propagation could arrest the crack propagation and play a significant role in protecting bone from damage. According to the examination of the two models with various areal fraction and variable distribution of the pores, the cavities altered the crack propagation path, and raising the pores percentage reduced the maximum stress necessary to start crack propagation. The areal fraction of the osteons is one of the critical parameters in bone fractures as revealed by the analysis of the two models with varying areal fraction of osteons, which decreases due to disease and aging.

Sensitivity analysis revealed how much the modulus of elasticity, areal fraction, and strain energy release rate of cortical bone tissue components influence ultimate strength on a small-length scale. It was shown that the areal fraction of pores as the Haversian canals and strain energy release rate of the interstitial matrix had the highest and the lowest effect on ultimate strength, respectively. Quasi-static analysis of the three models revealed obvious variances in global behavior and crack propagation paths in each model. The developed models can be used to monitor crack growth and predict bone fractures to reduce fracture risks for clinical purposes.

CRediT authorship contribution statement

P. Allahyari: Writing – original draft, Formal analysis, Data curation. **M. Silani:** Writing – review & editing, Supervision, Software, Project administration, Methodology, Investigation, Formal analysis, Conceptualization. **V. Yaghoubi:** Writing – review & editing, Methodology, Investigation, Formal analysis. **P. Milovanovic:** Writing – review & editing, Methodology, Investigation. **F.N. Schmidt:** Writing – original draft, Methodology, Investigation, Formal analysis. **B. Busse:** Writing – review & editing, Resources, Data curation, Conceptualization. **M. Qwamizadeh:** Writing – review & editing, Writing – original draft, Supervision, Software, Resources, Project administration, Methodology, Investigation, Conceptualization.

Declaration of competing interest

The authors declare that they have no known competing financial interests or personal relationships that could have appeared to influence the work reported in this paper.

Data availability

Data will be made available on request.

Acknowledgments

The authors acknowledge the funding to the Interdisciplinary Competence Center for Interface Research (ICCIR) / Forum Medical Technology Health on behalf of the University Medical Center Hamburg-Eppendorf (UKE) and the Hamburg University of Technology (TUHH) to

FNS, BB, and MQ. MQ has been supported by a postdoctoral fellowship granted by the Alexander von Humboldt foundation.

References

Abdel-Wahab, A.A., 2011. Experimental and Numerical Analysis of Deformation and Fracture of Cortical Bone Tissue. Loughborough University.

Abdel-Wahab, A.A., Alam, K., Silberschmidt, V.V., 2011. Analysis of anisotropic viscoelastoplastic properties of cortical bone tissues. J. Mech. Behav. Biomed. Mater. 4, 807–820.

Abdel-Wahab, A.A., Maligno, A.R., Silberschmidt, V.V., 2012. Micro-scale modelling of bovine cortical bone fracture: analysis of crack propagation and microstructure using X-FEM. Comput. Mater. Sci. 52, 128–135.

Agnew, A.M., Stout, S.D., 2012. Brief communication: reevaluating osteoporosis in human ribs: the role of intracortical porosity. Am. J. Phys. Anthropol. 148, 462–466.

Bala, Y., Seeman, E., 2015. Bone's material constituents and their contribution to bone strength in health, disease, and treatment. Calcif. Tissue Int. 97, 308–326.

Baptista, R., Almeida, A., Infante, V., 2016. Micro-crack propagation on a biomimetic bone like composite material studied with the extended finite element method. Procedia Struct. Integr. 1, 18–25.

Bayraktar, H.H., Morgan, E.F., Niebur, G.L., Morris, G.E., Wong, E.K., Keaveny, T.M., 2004. Comparison of the elastic and yield properties of human femoral trabecular and cortical bone tissue. J. Biomech. 37, 27–35.

Belytschko, T., Black, T., 1999. Elastic crack growth in finite elements with minimal remeshing. Int. J. Numer. Methods Eng. 45, 601–620.

Bernhard, A., Milovanovic, P., Zimmermann, E., Hahn, M., Djonic, D., Krause, M., et al., 2013. Micro-morphological properties of osteons reveal changes in cortical bone stability during aging, osteoporosis, and bisphosphonate treatment in women. Osteoporos. Int. 24, 2671–2680.

Bonivtch, A.R., Bonewald, L.F., Nicolella, D.P., 2007. Tissue strain amplification at the osteocyte lacuna: a microstructural finite element analysis. J. Biomech. 40, 2199–2206.

Bosnić, Z., Kononenko, I., 2008. Estimation of individual prediction reliability using the local sensitivity analysis. Appl. Intell. 29, 187–203.

Boyde, A., Hendel, P., Hendel, R., Maconnachie, E., Jones, S., 1990. Human cranial bone structure and the healing of cranial bone grafts: a study using backscattered electron imaging and confocal microscopy. Anat. Embryol. 181, 235–251.

Budyn, E., Hoc, T., 2006. Multi-scale modeling of human cortical bone: aging and failure studies. MRS Online Proc. Libr. 975, 1–6.

Burr, D.B., Schaffler, M.B., Frederickson, R.G., 1988. Composition of the cement line and its possible mechanical role as a local interface in human compact bone. J. Biomech. 21, 939–945.

Busse, B., Hahn, M., Soltau, M., Zustin, J., Püschel, K., Duda, G.N., et al., 2009. Increased calcium content and inhomogeneity of mineralization render bone toughness in osteoporosis: mineralization, morphology and biomechanics of human single trabeculae. Bone 45, 1034–1043.

Busse, B., Djonic, D., Milovanovic, P., Hahn, M., Püschel, K., Ritchie, R.O., et al., 2010. Decrease in the osteocyte lacunar density accompanied by hypermineralized lacunar occlusion reveals failure and delay of remodeling in aged human bone. Aging Cell 9, 1065–1075.

Cowin, S.C., Hegedus, D., 1976. Bone remodeling I: theory of adaptive elasticity. J. Elasticity 6, 313–326.

Currey, J.D., 1984. The Mechanical Adaptations of Bones. Princeton University Press, Princeton.

Currey, J.D., 1988. The effect of porosity and mineral content on the Young's modulus of elasticity of compact bone. J. Biomech. 21, 131–139.

Currey, J.D., 2002. Bones: Structure and Mechanics. Princeton University Press, Princeton.

De Pauw, D.J., Vanrolleghem, P.A., 2003. Practical Aspects of Sensitivity Analysis for Dynamic Models.

De Pauw, D.J., Vanrolleghem, P.A., 2005. Using the complex-step derivative approximation method to calculate local sensitivity functions of highly nonlinear bioprocess models. In: Proceedings 17th IMACS World Congress on Scientific Computation, Applied Mathematics and Simulation (IMACS 2005). Paris, France.

Demirtas, A., Curran, E., Ural, A., 2016. Assessment of the effect of reduced compositional heterogeneity on fracture resistance of human cortical bone using finite element modeling. Bone 91, 92–101.

Diehl, P., Lipton, R., Wick, T., Tyagi, M., 2022. A comparative review of peridynamics and phase-field models for engineering fracture mechanics. Comput. Mech. 1–35.

Giner, E., Belda, R., Arango, C., Vercher-Martínez, A., Tarancón, J.E., Fuenmayor, F.J., 2017. Calculation of the critical energy release rate Gc of the cement line in cortical bone combining experimental tests and finite element models. Eng. Fract. Mech. 184, 168–182.

Gustafsson, A., Khayyeri, H., Wallin, M., Isaksson, H., 2019a. An interface damage model that captures crack propagation at the microscale in cortical bone using XFEM. J. Mech. Behav. Biomed. Mater. 90, 556–565.

Gustafsson, A., Wallin, M., Khayyeri, H., Isaksson, H., 2019b. Crack propagation in cortical bone is affected by the characteristics of the cement line: a parameter study using an XFEM interface damage model. Biomech. Model. Mechanobiol. 18, 1247–1261.

Hahn, M., Vogel, M., Delling, G., 1991. Undecalcified preparation of bone tissue: report of technical experience and development of new methods. Virchows Arch. 418, 1–7.

Hamdia, K.M., Silani, M., Zhuang, X., He, P., Rabczuk, T., 2017. Stochastic analysis of the fracture toughness of polymeric nanoparticle composites using polynomial chaos expansions. Int. J. Fract. 206, 215–227.

Hernlund, E., Svedbom, A., Ivergård, M., Compston, J., Cooper, C., Stenmark, J., et al., 2013. Osteoporosis in the European Union: medical management, epidemiology and economic burden. Archives of osteoporosis 8, 136.

Idkaidek, A., Jasiuk, I., 2017. Cortical bone fracture analysis using XFEM-case study. Int. j. num. method. biomed. eng. 33, e2809.

Jirásek, M., 2000. Comparative study on finite elements with embedded discontinuities. Comput. Methods Appl. Mech. Eng. 188, 307–330.

Kaya, S., Basta-Pljakic, J., Seref-Ferlengez, Z., Majeska, R.J., Cardoso, L., Bromage, T.G., et al., 2017. Lactation-induced changes in the volume of osteocyte lacunar-canalicular space alter mechanical properties in cortical bone tissue. J. Bone Miner. Res. 32, 688–697.

Kingsmill, V., Boyde, A., 1998. Mineralisation density of human mandibular bone: quantitative backscattered electron image analysis. J. Anat. 192, 245–256.

Koehne, T., Marshall, R.P., Jeschke, A., Kahl-Nieke, B., Schinke, T., Amling, M., 2013. Osteopetrosis, osteopetrorickets and hypophosphatemic rickets differentially affect dentin and enamel mineralization. Bone 53, 25–33.

Koehne, T., Vettorazzi, E., Küsters, N., Lüneburg, R., Kahl-Nieke, B., Püschel, K., et al., 2014. Trends in trabecular architecture and bone mineral density distribution in 152 individuals aged 30-90 years. Bone 66, 31–38.

Koester, K., Barth, H., Ritchie, R., 2011. Effect of aging on the transverse toughness of human cortical bone: evaluation by R-curves. J. Mech. Behav. Biomed. Mater. 4, 1504–1513.

Lakes, R., Saha, S., 1979. Cement line motion in bone. Science 204, 501–503.

Li, S., 2013. Cutting of Cortical Bone Tissue: Analysis of Deformation and Fracture Process. Loughborough University.

Li, S., Abdel-Wahab, A., Silberschmidt, V.V., 2013. Analysis of fracture processes in cortical bone tissue. Eng. Fract. Mech. 110, 448–458.

Li, S., Abdel-Wahab, A., Demirci, E., Silberschmidt, V.V., 2014. Fracture process in cortical bone: X-FEM analysis of microstructured models. Fract. phenomena nat. technol.: Springer 43–55.

Miehe, C., Welschinger, F., Hofacker, M., 2010. Thermodynamically consistent phase-field models of fracture: variational principles and multi-field FE implementations. Int. J. Numer. Methods Eng. 83, 1273–1311.

Milovanovic, P., Rakocevic, Z., Djonic, D., Zivkovic, V., Hahn, M., Nikolic, S., et al., 2014. Nano-structural, compositional and micro-architectural signs of cortical bone fragility at the superolateral femoral neck in elderly hip fracture patients vs. healthy aged controls. Exp. Gerontol. 55, 19–28.

Milovanovic, P., Zimmermann, E.A., Riedel, C., vom Scheidt, A., Herzog, L., Krause, M., et al., 2015. Multi-level characterization of human femoral cortices and their underlying osteocyte network reveal trends in quality of young, aged, osteoporotic and antiresorptive-treated bone. Biomaterials 45, 46–55.

Milovanovic, P., Vom Scheidt, A., Mletzko, K., Sarau, G., Püschel, K., Djuric, M., et al., 2018. Bone tissue aging affects mineralization of cement lines. Bone 110, 187–193.

Mischinski, S., Ural, A., 2011. Finite Element Modeling of Microcrack Growth in Cortical Bone.

Moës, N., Dolbow, J., Belytschko, T., 1999. A finite element method for crack growth without remeshing. Int. J. Numer. Methods Eng. 46, 131–150.

Mohsin, S., O'Brien, F.J., Lee, T.C., 2006. Osteonal crack barriers in ovine compact bone. J. Anat. 208, 81–89.

Mulhern, D.M., 2000. Rib remodeling dynamics in a skeletal population from Kulubnarti, Nubia. Am. J. Phys. Anthropol.: The Off. Publ. American Association of Phys. Anthropol. 111, 519–530.

Najafi, A.R., Arshi, A.R., Eslami, M., Fariborz, S., Moeinzadeh, M.H., 2007. Micromechanics fracture in osteonal cortical bone: a study of the interactions between microcrack propagation, microstructure and the material properties. J. Biomech. 40, 2788–2795.

Najafi, A.R., Arshi, A.R., Saffar, K.P., Eslami, M.R., Fariborz, S., Moeinzadeh, M.H., 2009. A fiber-ceramic matrix composite material model for osteonal cortical bone fracture micromechanics: solution of arbitrary microcracks interaction. J. Mech. Behav. Biomed. Mater. 2, 217–223.

Nalla, R., Stölken, J., Kinney, J., Ritchie, R., 2005. Fracture in human cortical bone: local fracture criteria and toughening mechanisms. J. Biomech. 38, 1517–1525.

Nalla, R., Kruzic, J., Kinney, J., Balooch, M., Ager Iii, J., Ritchie, R., 2006. Role of microstructure in the aging-related deterioration of the toughness of human cortical bone. Mater. Sci. Eng. C 26, 1251–1260.

Nicolella, D.P., Moravits, D.E., Gale, A.M., Bonewald, L.F., Lankford, J., 2006. Osteocyte lacunae tissue strain in cortical bone. J. Biomech. 39, 1735–1743.

Osher, S., Sethian, J.A., 1988. Fronts propagating with curvature-dependent speed: algorithms based on Hamilton-Jacobi formulations. J. Comput. Phys. 79, 12–49.

O'Brien, F.J., Taylor, D., Lee, T.C., 2003. Microcrack accumulation at different intervals during fatigue testing of compact bone. J. Biomech. 36, 973–980.

Pandolfi, A., Ortiz, M., 2012. An eigenerosion approach to brittle fracture. Int. J. Numer. Methods Eng. 92, 694–714.

Pistoia, W., van Rietbergen, B., Rüegsegger, P., 2003. Mechanical consequences of different scenarios for simulated bone atrophy and recovery in the distal radius. Bone 33, 937–945.

Rabczuk, T., Belytschko, T., 2004. Cracking particles: a simplified meshfree method for arbitrary evolving cracks. Int. J. Numer. Methods Eng. 61, 2316–2343.

Rabczuk, T., Zi, G., Gerstenberger, A., Wall, W.A., 2008. A new crack tip element for the phantom-node method with arbitrary cohesive cracks. Int. J. Numer. Methods Eng. 75, 577–599.

Rabczuk, T., Zi, G., Bordas, S., Nguyen-Xuan, H., 2010. A simple and robust three-dimensional cracking-particle method without enrichment. Comput. Methods Appl. Mech. Eng. 199, 2437–2455.

Rakovec, O., Hill, M.C., Clark, M., Weerts, A., Teuling, A., Uijlenhoet, R., 2014. Distributed evaluation of local sensitivity analysis (DELSA), with application to hydrologic models. Water Resour. Res. 50, 409–426.
Rho, J.Y., Zioupos, P., Currey, J.D., Pharr, G.M., 2002. Microstructural elasticity and regional heterogeneity in human femoral bone of various ages examined by nano-indentation. J. Biomech. 35, 189–198.
Riedel, C., Zimmermann, E.A., Zustin, J., Niecke, M., Amling, M., Grynpas, M., et al., 2017. The incorporation of fluoride and strontium in hydroxyapatite affects the composition, structure, and mechanical properties of human cortical bone. J. Biomed. Mater. Res. 105, 433–442.
Roschger, P., Fratzl, P., Eschberger, J., Klaushofer, K., 1998. Validation of quantitative backscattered electron imaging for the measurement of mineral density distribution in human bone biopsies. Bone 23, 319–326.
Schaffler, M.B., Burr, D.B., Frederickson, R.G., 1987. Morphology of the osteonal cement line in human bone. Anat. Rec. 217, 223–228.
Schmidt, F.N., Zimmermann, E.A., Campbell, G.M., Sroga, G.E., Püschel, K., Amling, M., et al., 2017. Assessment of collagen quality associated with non-enzymatic cross-links in human bone using Fourier-transform infrared imaging. Bone 97, 243–251.
Schmidt, F.N., Delsmann, M.M., Mletzko, K., Yorgan, T.A., Hahn, M., Siebert, U., et al., 2018. Ultra-high matrix mineralization of sperm whale auditory ossicles facilitates high sound pressure and high-frequency underwater hearing. Proc. Royal Soc. B 285, 20181820.
Schmidt, F.N., Zimmermann, E.A., Walsh, F., Plumeyer, C., Schaible, E., Fiedler, I.A., et al., 2019. On the origins of fracture toughness in advanced teleosts: how the swordfish sword's bone structure and composition allow for slashing under water to kill or stun prey. Adv. Sci. 6, 1900287.
Silling, S.A., 2000. Reformulation of elasticity theory for discontinuities and long-range forces. J. Mech. Phys. Solid. 48, 175–209.
Silling, S.A., Lehoucq, R.B., 2010. Peridynamic theory of solid mechanics. Adv. Appl. Mech. 44, 73–168.
Silling, S.A., Epton, M., Weckner, O., Xu, J., Askari, E., 2007. Peridynamic states and constitutive modeling. J. Elasticity 88, 151–184.
Skedros, J.G., Holmes, J.L., Vajda, E.G., Bloebaum, R.D., 2005. Cement lines of secondary osteons in human bone are not mineral-deficient: new data in a historical perspective. Anat. Rec. Part A: Discoveries in Molecular, Cellular, and Evolutionary Biology: An Official Publication of the American Association of Anatomists 286, 781–803.
Stockhausen, K.E., Qwamizadeh, M., Wölfel, E.M., Hemmatian, H., Fiedler, I.A., Flenner, S., et al., 2021. Collagen fiber orientation is coupled with specific nano-compositional patterns in dark and bright osteons modulating their biomechanical properties. ACS Nano 15, 455–467.
Vu-Bac, N., Lahmer, T., Zhuang, X., Nguyen-Thoi, T., Rabczuk, T., 2016. A software framework for probabilistic sensitivity analysis for computationally expensive models. Adv. Eng. Software 100, 19–31.
Wang, M., Zimmermann, E.A., Riedel, C., Busse, B., Li, S., Silberschmidt, V.V., 2017. Effect of micro-morphology of cortical bone tissue on fracture toughness and crack propagation. Procedia Struct. Integr. 6, 64–68.
Wang, M., Li, S., vom Scheidt, A., Qwamizadeh, M., Busse, B., Silberschmidt, V.V., 2020. Numerical study of crack initiation and growth in human cortical bone: effect of micro-morphology. Eng. Fract. Mech. 232, 107051.
Xu, X.-P., Needleman, A., 1994. Numerical simulations of fast crack growth in brittle solids. J. Mech. Phys. Solid. 42, 1397–1434.
Yoshino, M., Imaizumi, K., Miyasaka, S., Seta, S., 1994. Histological estimation of age at death using microradiographs of humeral compact bone. Forensic Sci. Int. 64, 191–198.
Zimmermann, E.A., Ritchie, R.O., 2015. Bone as a structural material. Adv. healthcare mater. 4, 1287–1304.
Zimmermann, E.A., Launey, M.E., Barth, H.D., Ritchie, R.O., 2009. Mixed-mode fracture of human cortical bone. Biomaterials 30, 5877–5884.
Zimmermann, E.A., Schaible, E., Bale, H., Barth, H.D., Tang, S.Y., Reichert, P., et al., 2011. Age-related changes in the plasticity and toughness of human cortical bone at multiple length scales. Proc. Natl. Acad. Sci. USA 108, 14416–14421.
Zimmermann, E.A., Gludovatz, B., Schaible, E., Busse, B., Ritchie, R.O., 2014. Fracture resistance of human cortical bone across multiple length-scales at physiological strain rates. Biomaterials 35, 5472–5481.
Zimmermann, E.A., Busse, B., Ritchie, R.O., 2015. The fracture mechanics of human bone: influence of disease and treatment. BoneKEy Rep. 4.
Zimmermann, E.A., Schaible, E., Gludovatz, B., Schmidt, F.N., Riedel, C., Krause, M., et al., 2016. Intrinsic mechanical behavior of femoral cortical bone in young, osteoporotic and bisphosphonate-treated individuals in low-and high energy fracture conditions. Sci. Rep. 6, 1–12.